Spatiotemporal changes in seismic velocity associated with hydraulic fracturing-induced earthquakes near Fox Creek, Alberta, Canada

Adebayo Oluwaseun Ojo[a, *], Honn Kao[a,b], Ryan Visser[a,c], and Chet Goerzen[b]
[a]Geological Survey of Canada, Natural Resources Canada, Sidney, British Columbia, Canada
[b]School of Earth and Ocean Sciences, University of Victoria, Victoria, British Columbia, Canada
[c]Geoscience BC, Vancouver, British Columbia, Canada

*Corresponding author: Adebayo Ojo (ojo.adebayo.oluwaseun@gmail.com; adebayo.ojo@canada.ca)

Abstract

To characterize the subsurface geomechanical response to hydraulic fracturing activities, we study the spatiotemporal changes of seismic velocity during the completion of four injection wells in the Fox Creek area, Alberta, Canada. We estimate temporal velocity changes (dv/v) from ambient seismic noise recorded during the Tony Creek Dual Microseismic Experiment (ToC2ME) by comparing a 5-day stacked noise correlation function with a reference noise correlation function stacked over the deployment period. In the frequency band (0.1 - 0.4 Hz) most sensitive to the injection depths (~3.4 km), we observe daily dv/v that revealed alternating gradual velocity decreases and increases with magnitudes in the range of ±0.9%. We found a strong temporal correlation between the onset of velocity decreases and periods of intense seismicity, suggesting that the observed dv/v reductions are likely caused by stress-induced subsurface deformation due to elevated pore pressures, increased crack density, and ground shaking. A period of dv/v increase observed between the beginning and end of different well stimulation is attributed to crustal healing. Comparing the dv/v time series with injection parameters, we observed a 272.66% increase in induced seismicity and 50% more reduction in dv/v during the second injection phase that are correlated with 90.53%, 169.64%, and 4.34% increase in the injection volume, rate, and pressure, respectively. Our study provides valuable new information on the changes in reservoir elastic properties within the Western Canadian Sedimentary Basin. It also demonstrates that coda wave interferometry using data from dense seismic arrays near injection sites can be an additional tool for monitoring hydraulic fracturing operations.

Keywords: Hydraulic Fracturing, Coda wave Interferometry, Seismic Noise, Temporal Velocity Change

1. Introduction

Hydraulic fracturing (HF) is a novel technology for enhancing subsurface permeability of hydrocarbon reservoirs, geothermal systems, and underground mines to increase productivity. It typically involves the injection of fluids under high pressure through a wellbore into a targeted formation to create fractures which subsequently serve as conduits to extract the trapped resources (Schultz et al., 2017, 2018, 2020). Although this process can yield increased economic benefits and reduced environmental footprints, it is poised with the risk of generating felt and damaging earthquakes (Ellsworth, 2013; Pezzo et al., 2018; Kao et al., 2018a). Within the Western Canadian Sedimentary Basins (WCSB), HF activities have been identified as the primary driver of increasing seismicity since 2010, including the largest induced event (M4.6) on August 17, 2015, in the northern Montney Play (e.g., Ghofrani and Atkinson, 2016; Babaie Mahani et al., 2017; Schultz et al., 2018,2020; Hui et al., 2021). Long-term analysis of earthquakes within the WCSB revealed that ~62% of earthquakes with M≥3 from 2010-2015 were associated with HF compared to only ~8.5% before 2010 (Atkinson et al., 2016, 2020; Ghofrani and Atkinson, 2020). Increasing concerns from both society and the governments result in several regulatory procedures being enacted to guide HF operations (e.g., traffic light protocol; AER, 2015; Kao et al., 2016, 2018b) and mitigate the potential seismic risk. Adherence to these operational standards will benefit enormously from monitoring the subsurface response to ongoing HF activities continuously (e.g., Qin et al., 2020; Yu et al., 2020; Zhang et al., 2020). Likewise, understanding the causative mechanism of any physical changes in the subsurface makes it possible to improve the assessment of seismic hazards due to induced earthquakes (Kortink, 2020). Therefore, novel and cost-effective ways of monitoring the subsurface during high-pressure fluid injection and HF operations are highly sought after to guide well operations and reduce the probability of generating induced earthquakes large enough to cause damage (Civilini et al., 2020).

Generally, it is difficult to measure changes in pressure without direct access to the targeted formation. Hence remote measurements of any Earth property that can indirectly provide information about subsurface pressure are highly valuable. For many years, seismologist have used seismic velocity to reveal the internal state of the Earth, and several experiments have shown its high sensitivity to stress perturbation due to fluid pressure within the subsurface (e.g., Olivier and Brenguier, 2016; Amann et al., 2018; Doetsch et al., 2018). Temporal behaviors of fluids in the subsurface can be detected and monitored by remotely measuring the time-lapse changes in seismic velocity at seismogenic depths (Grêt et al., 2006; Niu et al., 2008; Clarke et al., 2011; Tribaldos and Ajo-Franklin, 2021). To achieve this, several seismological methods have been developed that use a variety of sources (e.g., active source, repeating earthquakes, and ambient seismic noise) and can be applied to a wide range of applications (e.g., volcanoes, geothermal reservoirs, earthquakes, underground mines, landslides, active faults, earth dams, seasonal cycles, precipitations, and water table fluctuations) and reported in the literature (e.g., Ikuta and Yamaoka, 2004; Chadwick et al., 2010; Nakata and Snieder, 2012; Roux and Ben-Zion, 2013; Froment et al., 2013; Mordret et al., 2016; James et al., 2017; Wang et al., 2017; Lecocq et al., 2017; Clements and Denolle, 2018; Hillers et al., 2019; Qiu et al., 2020). However, due to the more recent advancement in seismic interferometry (e.g., Lobkis and Weaver, 2001; Shapiro and Campillo, 2004), increasing deployments of dense seismic networks (e.g., Eaton et al., 2018) and the development of efficient algorithms for data processing (e.g., Lecocq et al., 2014), the passive seismic ambient noise method is widely favored for continuous monitoring of temporal velocity changes at unprecedented precision and temporal resolution (e.g., Brenguier et al., 2008, 2014, 2016; Froment et al., 2013; Obermann et al., 2014; Hobiger et al., 2016; Taira and Brenguier, 2016; Mao et al., 2019; De Plaen et al., 2019; Yates et al., 2019). Based on this method, noticeable reduction in seismic velocities in the order of a fraction of a percent (~ 1%) have been reported to precede the eruption of volcanoes (De Plaen et al., 2016; Olivier et al., 2019; Wu et al., 2020), sharp velocity drops are observed to have coincided with the occurrence of large magnitude earthquakes (e.g., Taira et al., 2015; Wu et al., 2016; Yukutake et al., 2016; Pei et al., 2019), and velocity perturbations related to meteorological conditions (temperature, rainfall, groundwater, snow, frost, and atmospheric pressure) are documented (e.g., Lecocq et al., 2017). This approach is also suitable for monitoring HF and fluid injection-induced velocity changes, and a handful of case studies have been published that reveal near-well velocity reductions (e.g., Doetsch et al., 2018; Taira et al., 2018; Vaezi and Van der Baan, 2019; Zhang et al., 2020).

Being a relatively new type of measurement, delineation of the detailed spatiotemporal velocity changes and the underlying physical mechanisms are not yet fully understood. Further advance would require studies using newly available data from dense seismic networks deployed near the deformation source. Specifically, for fluid injection and HF, it is not yet fully understood how fluid pressure within the Earth's crust evolves over time and triggers induced earthquakes via fault reactivation or aseismic deformation (e.g., Wang et al., 2017; Doetsch et al., 2018; Igonin et al., 2020). Therefore, in this study, we investigate the temporal velocity changes during the completion of four HF wells in the Fox Creek area, Alberta, Canada using ambient seismic noise data recorded by a dense seismic network with full azimuthal coverage around the wellbore. Our goal is to detect spatiotemporal changes in seismic velocity related to the HF activities, understand their causative mechanisms, and investigate their relationships to other observations, such as induced seismicity, ground motions, and injection parameters. We also seek to understand the potential of using coda wave interferometry to understand the subsurface changes that might induce earthquakes.

2. Data and Method

We retrieved continuous ambient seismic noise data recorded by sixty-nine (69) three-component shallow-buried 10 Hz geophones, six (6) broadband seismometers, and one (1) strong-motion accelerometer deployed during the Tony Creek Dual Microseismic Experiment (ToC2ME) from the Incorporated Research Institutions for Seismology (IRIS) Data Management Center (e.g., Eaton et al., 2018; Igonin et al., 2018, 2020; Fig. 1). The ToC2ME array recorded data for ~37 days (October 26, 2016 - December 1, 2016) and was deployed around 4 HF wells within a radius of ~8 km. The HF injection was performed at a depth of ~3,400 m within the Kaybob-Duvernay horizon in the Fox Creek area, Alberta. When conducting this study, the geophones' instrument response information is incorrect, so we use data from the six broadband seismometers and the accelerometer to investigate possible ground shaking due to HF-induced earthquakes. For further analysis, we use a published catalog with ~18,039 induced events recorded from October 25, 2016, to November 30, 2016 (Igonin et al., 2020). Also, we use well completions and fracture data obtained from the geoLOGIC database (e.g., Eaton et al., 2018).

We use the Python package MSNoise (Lecocq et al., 2014) and follow the established workflow to pre-process the raw data, perform ambient noise correlation and estimate the seismic velocity changes (e.g., Brenguier et al., 2008; Taira et al., 2015, 2018). Specifically, we first down-sample the raw waveform to 20 Hz and apply a bandpass filter between 0.01 and 8.0 Hz. Subsequently, the waveform is divided into 30-minute time segments with the mean and trend removed. Next, we perform one-bit normalization and spectral whitening to suppress seismic signals related to earthquakes and monochromatic noise sources (e.g., Bensen et al., 2007; Larose et al., 2004; Lecocq et al., 2017). The same geophones (OYO GSX-3 sensors) were used at all stations, so instrument responses are expected to be stable over time, making instrument corrections unnecessary. We compute the cross-correlation between the vertical-vertical (ZZ) components using all the stations in a 30-minute window with 90% overlap, and we linearly stack the noise correlation functions (NCFs) for each station-pair to obtain a daily stack for a lapse time between -50 and +50 s. Likewise, we linearly stack all the NCFs for each station-pair during the entire deployment period to obtain reference NCFs (see Fig. S1). To enhance the signal-to-noise ratio (SNR) and suppress the effect of non-isotropic noise sources, we merged the causal and acausal sides of the NCFs for subsequent velocity change (dv/v) measurements.

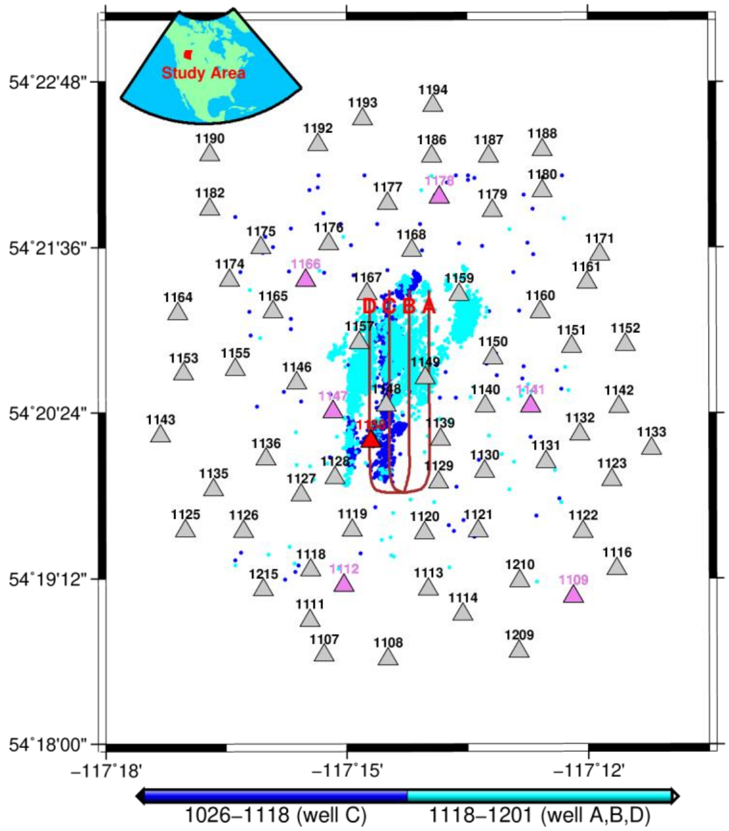

Fig. 1. Map of the study area showing the seismic network, hydraulic fracturing wells (A, B, C, and D), and induced earthquakes (Igonin et al., 2020). Triangles colored in violet and red show the location of the six broadband seismic stations and the accelerometer, respectively. They are co-located with the 69 shallow-buried geophones shown in gray-colored triangles. The blue-colored circles show the induced earthquakes recorded during the stimulation of well C from 2016-10-26 to 2016-11-18 while the cyan-colored circles denote the stimulation involving wells A, B, and D from 2016-11-18 to 2016-12-01. The insert map shows the geographical location of the study area on the map of North America.

The estimation of dv/v from NCFs is fast developing, and several methods with varying advantages and disadvantages have been published (e.g., Lobkis and Weaver 2003; Clarke et al. 2011; Mikesell et al. 2015; Mao et al. 2019; Taylor and Hillers, 2020). We test both the frequency-domain Moving-Window Cross-Spectrum (MWCS) method (Poupinet et al. 1984; Clarke et al., 2011) and the time-domain stretching interpolation (STR) method (Lobkis and Weaver 2003; Sens-Schönfelder and Wegler 2006). It turns out that, in our case, the STR method can deliver a more stable and precise result with fewer fluctuations when optimally dilated waveforms are used, similar to other successful applications (e.g., Sens-Schönfelder and Larose, 2008, Hadziioannou et al., 2009, 2011; Yukutake et al., 2016; Nimiya et al., 2017; Tribaldos and Ajo-Franklin, 2021). For this method, the current NCFs (which are more sensitive to the current state of the subsurface) or the reference NCF (which is sensitive to the average state of the subsurface) are dilated or compressed in a selected time window in the time domain, and the stretching coefficient (δ_s) that gives the maximum correlation coefficient between them is determined via a grid search. To prevent direct wave contamination, we measure the time delays using 30-s-long data in the coda wave window (5 - 35 s) of the NCFs, which are more sensitive to velocity changes and less affected by variations of noise sources (Snieder et al., 2002; Sens-Schönfelder and Wegler, 2006; Stehly et al., 2006). The reference NCF is the stack of all NCFs in the selected frequency band for the entire study period, and we compare it with the current NCF-stack of 1, 2, 5, 10, 15, 20, and 30 days to investigate the trade-off between SNR and temporal resolution. If we assume that the surface waves are evenly distributed and scattered, as well as a homogenous velocity perturbation, then the obtained δ_s for a specified time lag (τ) is proportional to the apparent velocity change (dv/v) in the medium (i.e., $dv/v = -d\tau/\tau$ and $dv/v = \delta_s - 1$) (e.g., Ratdomopurbo and Poupinet, 1995; Snieder et al., 2002; Brenguier et al., 2008). To ensure that stable NCFs are used in the study, only dv/v values with δ_s between the reference and current NCFs greater than 0.85 are accepted. Due to the relatively short data recording period (~37 days), the effect of seasonal variation of noise sources, which is reported to introduce apparent velocity changes when the STR method is used, is not of concern (e.g., Hadziioannou et al., 2009; Zhan et al., 2013). The NCFs are computed in six (6) frequency bands (0.1-0.4 Hz; 0.2-0.5 Hz; 0.3-0.8 Hz; 0.4-0.9 Hz; 0.5-1.0 Hz, and 0.7-2.0 Hz) to enable the measurement of dv/v at different depths (e.g., Obermann et al., 2016).

3. Results

The dv/v is computed using a different number of days (1,2, 5, 10, 15, 20, 30) in the stacking process for the current NCFs, and we find that a minimum of 5 days is necessary to obtain a more stable result. Hence, we present the results of dv/v estimated by stretching or compressing a 5-day stacked current NCFs with a reference stacked over the deployment period. This approach enables us to track the velocity change evolution over a relatively short timescale. Fig. 2a shows the network-averaged daily dv/v measurements at various frequency bands (0.1-0.4, 0.2-0.5, 0.3-0.8, 0.4-0.9, 0.5-1.0, and 0.7-2.0 Hz). It reveals a frequency-dependent velocity change with the amplitude fluctuation most pronounced in the lowest frequency range (0.1-0.4 Hz) considered in the study. The amplitudes of dv/v are much reduced in higher frequency bands (e.g., 0.4-0.9, 0.5-1.0), and eventually disappear in the band of 0.7-2.0 Hz. Averaging the daily dv/v suppresses the background variations, and the reduced amplitudes at higher frequencies indicate that the potential velocity changes are indistinguishable from the background variations. The observed spatiotemporal evolution of the daily dv/v (Fig. 3) and the time history of the mean daily dv/v for all stations (Fig. 2a) show four distinct phases of velocity changes characterized by alternating decreases and increases with an average period of 5, 5-6, 12-16, 10-14 days respectively (see Fig. 2b).

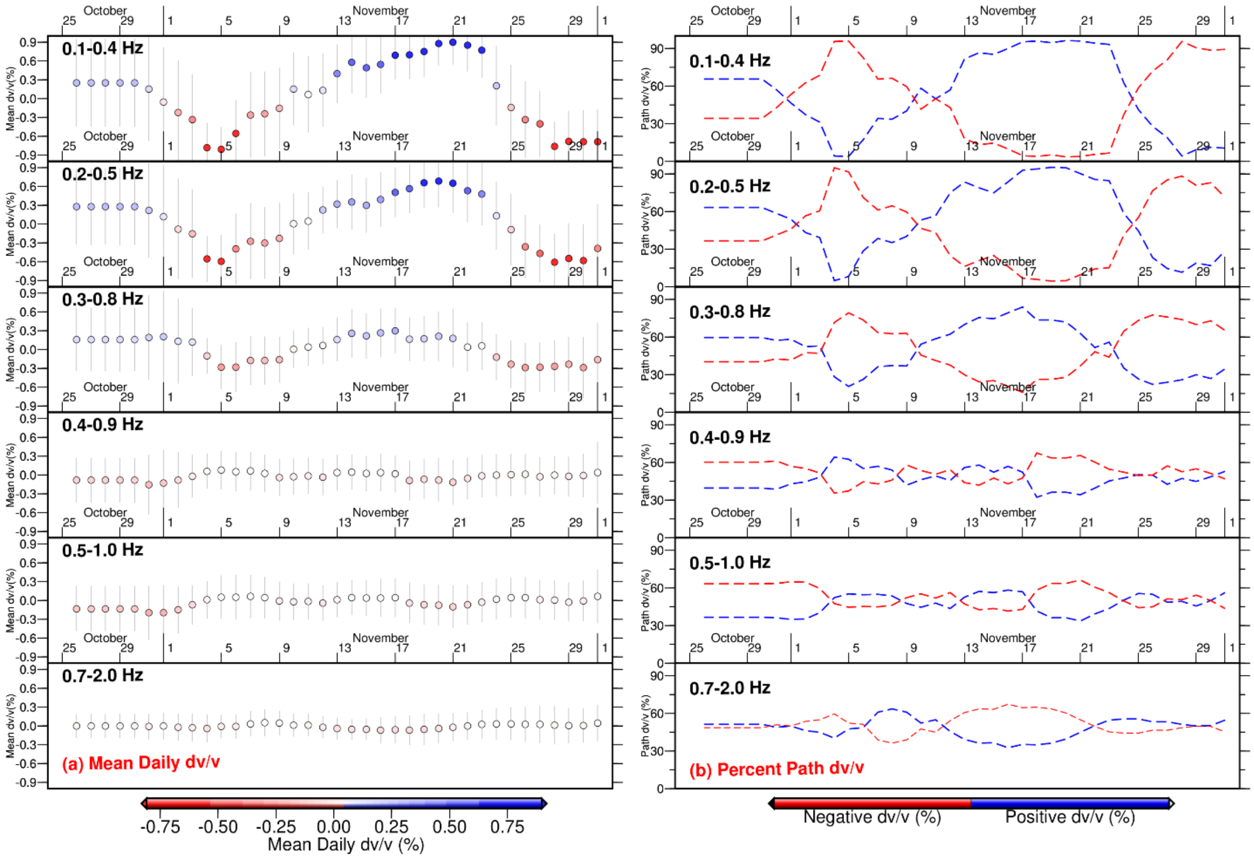

Fig. 2. Time history of temporal seismic velocity (dv/v) at six different frequency bands (0.1-0.4, 0.2-0.5, 0.3-0.8, 0.4-0.9, 0.5-1.0, and 0.7-2.0 Hz). (a) shows the network-averaged daily dv/v measurements and their standard deviation at different frequency bands over the deployment period (b) Percentage of station-pairs associated with velocity increases (>0%; blue dashed line) or decreases (< 0%; red dashed line) over the deployment period. The maximum number of the inter-station path is 2,346.

In the lowest frequency band where the velocity changes are most pronounced (i.e., 0.1-0.4 Hz), the mean daily dv/v ranges from -0.81% to 0.90% with a standard deviation of 0.35 to 0.87. From the onset of the experiment (October 26, 2016), the mean daily dv/v is ~0.26% and remains constant till October 30, 2016 (Fig. 2). The constant dv/v value at the beginning of the experiment may represent the background value or be caused by temporal resolution limitations. Using a 5-day stacked moving window may have limited our ability to observe changes at a smaller time scale distinctively. The mean daily dv/v began to decrease on October 31, 2016, reaching ~-0.81% on November 5, 2016. A sharp drop from -0.33% to -0.78% occurred from November 3 to 4, 2016. A healing phase started on November 6, 2016, i.e., dv/v began to increase gradually and eventually exceeded the background value. It reached ~0.90% on November 21, 2016, then dropped persistently to ~-0.76% on November 28, 2016. After that, it leveled out at ~-0.68% till the end of the survey on December 1, 2016.

Using 69 shallow-buried geophones, we obtain a total of 2,346 inter-station paths, sensitive to perturbations in the medium along the path connecting any two stations. The percentage of these paths that revealed either positive or negative velocity change can also provide some additional insight into the dominant process at various times during the deployment (see Fig. 2b). In Fig. 3, we show the spatiotemporal evolution of the dv/v across the study area for each day throughout the deployment period. The trend of the estimated percentages generally follows the same trend as the time evolution of the mean daily dv/v described above, revealing four distinct phases where dv/v alternates from positive (dv/v increases) to negative (dv/v decreases) in a transitional manner. For example, at 0.1-0.4 Hz, 65.64% and 34.36% of the inter-station paths are associated with positive and negative daily mean dv/v, respectively (Fig. 2b) between October 26 and 30, 2016. It suggests that a more significant portion of the study region is characterized by velocity increases in the first injection phase (Fig. 2b and Fig. 3). In the second injection phase (October 31 to November 5, 2016), most of the study area experienced velocity decreases with the percentage of inter-station paths indicating negative dv/v increasing from 34.36% to 96%. Subsequently, a healing phase began when the percentage of inter-station paths crosscutting the study area with positive dv/v increased from ~4% to ~96% over a relatively long period (from November 6 to 21, 2016). Following the healing phase was a relatively fast velocity reduction across almost the entire study area from November 22 to December 1, 2016 (Fig. 2b and Fig. 3). At higher frequencies considered in the study (e.g., 0.2-0.5 and 0.3-0.8 Hz), similar patterns of dv/v can be observed but with reduced amplitudes (see Fig. 2 and Fig. S2-S6).

4. Interpretation and Discussion

4.1 Depth Sensitivity of dv/v Measurements

Measuring the temporal seismic velocity change at various frequency bands with distinct sensitivities to different depths enables us to investigate the observed changes' origin and separate the effects of potential causal mechanisms. It is usually assumed that the early coda of the noise correlation functions is mainly composed of scattered surface waves (e.g., Obermann et al., 2013, 2016). Therefore, we compute the depth sensitivity of Rayleigh waves to a local 1-D shear wave velocity (Vs) model at several frequencies between 0.1 and 1.0 Hz (Levshin et al., 1989). The local velocity model was constructed from well-logs up to a depth of 3.5 km and crustal refraction profiles to a depth of 6 km (Zelt and Ellis, 1989; Tan et al., 2019).

As shown in Fig. 4a, the velocity changes computed at higher frequency (e.g., 1 Hz) are mainly sensitive to perturbations at depths less than 1 km below the surface, whereas dv/v at relatively lower frequencies (e.g., 0.1 Hz) are sensitive to perturbations in deeper structures (> 2 km). The most pronounced velocity changes were observed at relatively lower frequencies (0.1-0.4 and 0.2- 0.5 Hz), suggesting that the process responsible for the observed changes is most likely occurring at depths greater than 2 km beneath the study region (see Fig. 2a). Similar dv/v trends with varying amplitudes at the frequency bands considered in this study may indicate that the observed velocity changes extend over variable depth ranges. The depth estimates of the recorded induced events are between 2.0 and 4.5 km, and the reported depth of the four injection wells is between 3.4 and 3.5 km (Eaton et al., 2018; Poulin et a., 2019; Igonin et al., 2020).

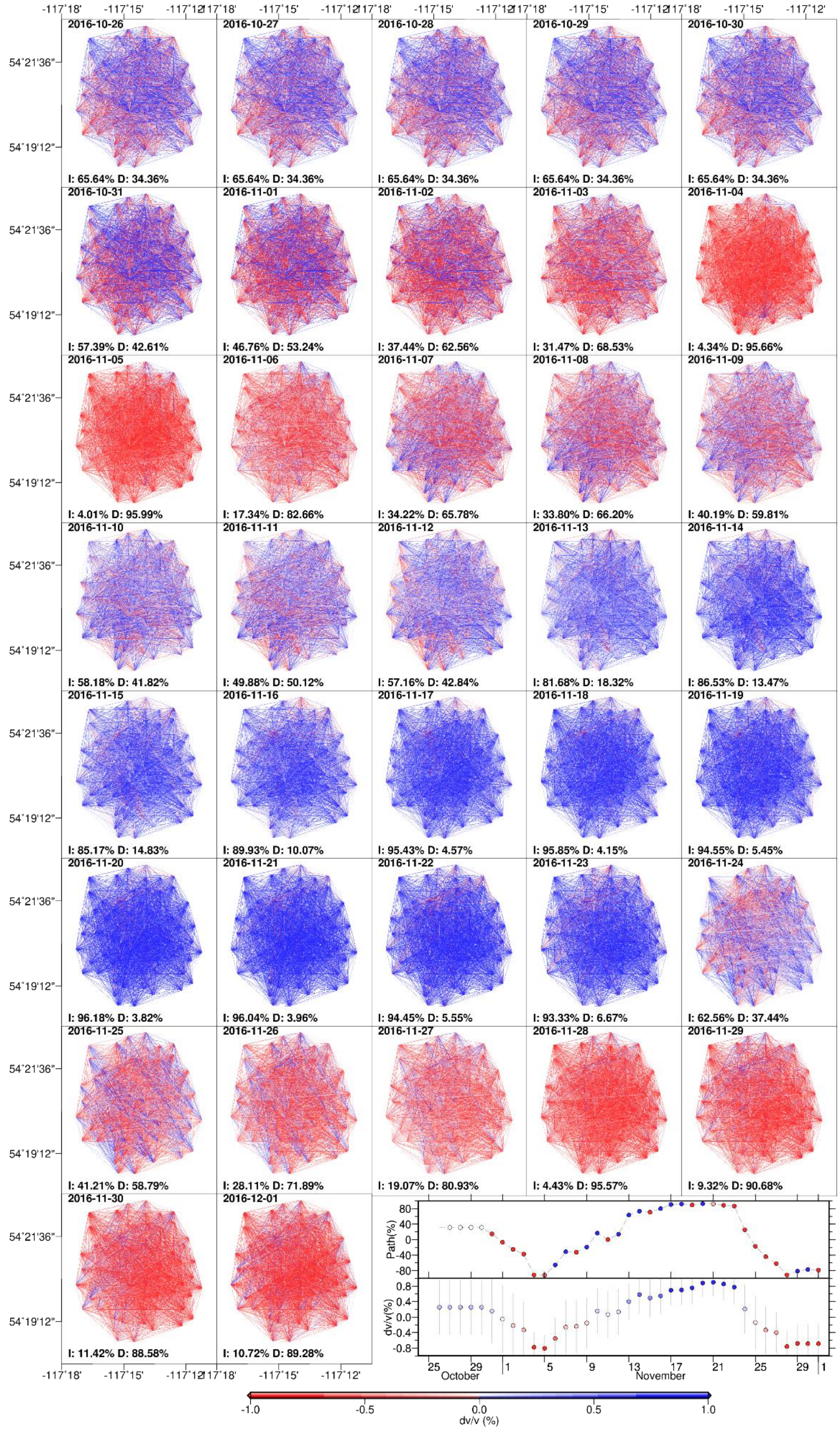

-117°18'
-117°15'
-117°12'
54°21'36"
54°19'12"
2016-10-26
I: 65.64% D: 34.36%
2016-10-27
I: 65.64% D: 34.36%
2016-10-28
I: 65.64% D: 34.36%
2016-10-29
I: 65.64% D: 34.36%
2016-10-30
I: 65.64% D: 34.36%
2016-10-31
I: 57.39% D: 42.61%
2016-11-01
I: 46.76% D: 53.24%
2016-11-02
I: 37.44% D: 62.56%
2016-11-03
I: 31.47% D: 68.53%
2016-11-04
I: 4.34% D: 95.66%
2016-11-05
I: 4.01% D: 95.99%
2016-11-06
I: 17.34% D: 82.66%
2016-11-07
I: 34.22% D: 65.78%
2016-11-08
I: 33.80% D: 66.20%
2016-11-09
I: 40.19% D: 59.81%
2016-11-10
I: 58.18% D: 41.82%
2016-11-11
I: 49.88% D: 50.12%
2016-11-12
I: 57.16% D: 42.84%
2016-11-13
I: 81.68% D: 18.32%
2016-11-14
I: 86.53% D: 13.47%
2016-11-15
I: 85.17% D: 14.83%
2016-11-16
I: 89.93% D: 10.07%
2016-11-17
I: 95.43% D: 4.57%
2016-11-18
I: 95.85% D: 4.15%
2016-11-19
I: 94.55% D: 5.45%
2016-11-20
I: 96.18% D: 3.82%
2016-11-21
I: 96.04% D: 3.96%
2016-11-22
I: 94.45% D: 5.55%
2016-11-23
I: 93.33% D: 6.67%
2016-11-24
I: 62.56% D: 37.44%
2016-11-25
I: 41.21% D: 58.79%
2016-11-26
I: 28.11% D: 71.89%
2016-11-27
I: 19.07% D: 80.93%
2016-11-28
I: 4.43% D: 95.57%
2016-11-29
I: 9.32% D: 90.68%
2016-11-30
I: 11.42% D: 88.58%
2016-12-01
I: 10.72% D: 89.28%
Path(%)
80
40
0
-40
-80
dv/v(%)
0.8
0.4
0.0
-0.4
-0.8
25
29
October
1
5
9
13
17
November
21
25
29
1
-1.0
-0.5
0.0
0.5
1.0
dv/v (%)

Fig. 3. Daily spatiotemporal evolution of dv/v throughout the deployment at 0.1-0.4 Hz. The colored lines show the inter-station paths across the study area and the associated dv/v measurement. Also shown are the daily averaged values like in Fig. 2. Plots at other frequency bands are presented in Fig. S2-S6.

The sensitivity kernel at the lower frequency bands (e.g., 0.1 - 0.4 Hz) where we observed the most significant dv/v perturbations has large values up to 4 km below the surface similar to the depths of the induced events and injection wells (Fig. 4b). The correlation between the depth sensitivity of the observed dv/v variation at this frequency band (0.1-0.4 Hz) and the depths of HF stimulation and induced earthquakes provides the first indication that the observed dv/v is most likely related to subsurface perturbations associated with HF injections.

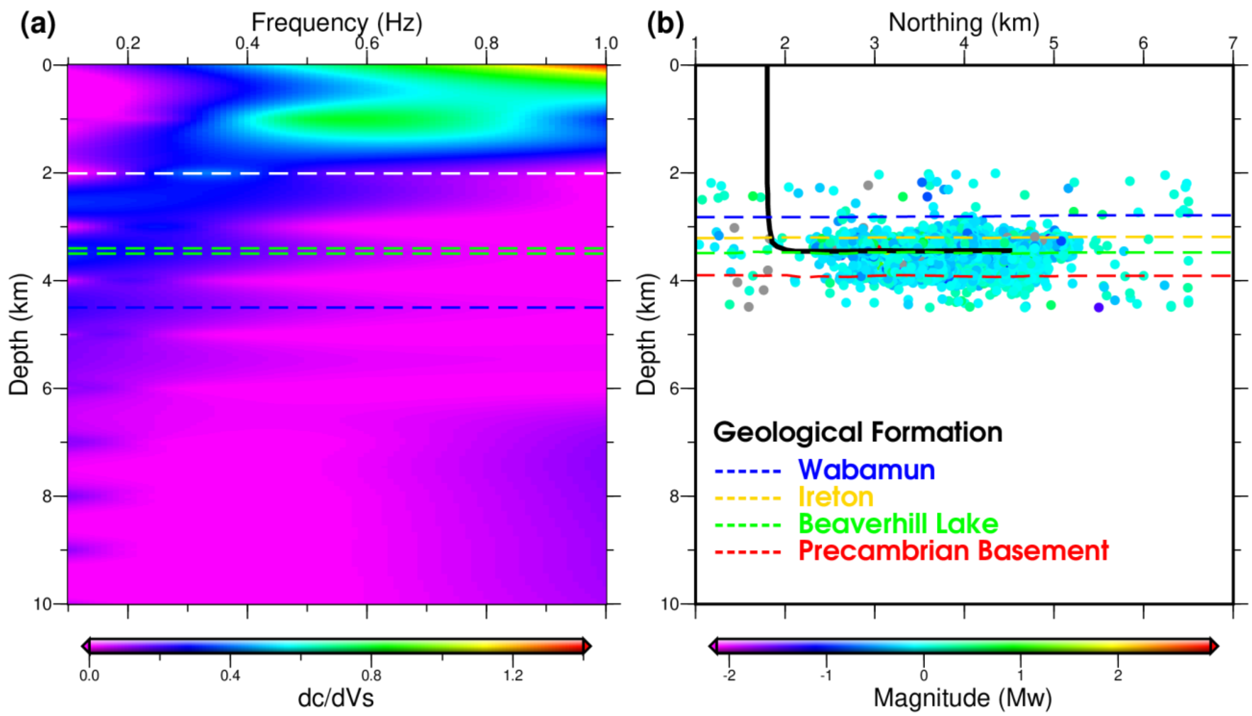

Fig. 4. (a) Sensitivity kernel of Rayleigh wave to 1-D local velocity model at different frequencies ranging from 0.1-1 Hz. The corresponding sensitivity kernels are the derivative of the Rayleigh wave phase velocity to the S wave velocity at various frequencies. As expected, the depth of the highest sensitivity increases as frequency decreases. White and blue dash lines show the depth range of induced earthquakes, and green dash lines show the injection depth range. (b) The depth distribution of induced events (Igonin et al., 2020) with colors indicating event magnitudes. The horizontal dashed lines show the top boundary of different geological formations (Eaton et al., 2018).

4.2 Origin and Causative Mechanism of the observed dv/v

Spatiotemporal changes in the seismic velocity are typically controlled by various factors and natural internal processes, such as stress, deformation, fluids, and meteorological conditions. Therefore, understanding the exact mechanisms causing changes in dv/v is often challenging because of the difficulty in isolating the contribution from individual effects (e.g., Sens-Schönfelder et al., 2014; Donaldson et al., 2017). To investigate the causative mechanism of the observed dv/v, we compare the time evolution of the daily mean dv/v to the temporal evolution of induced seismicity, daily injection parameters (average pumping pressure, average pumping rate, injected volume), and daily peak ground acceleration (PGA) in Fig. 5.

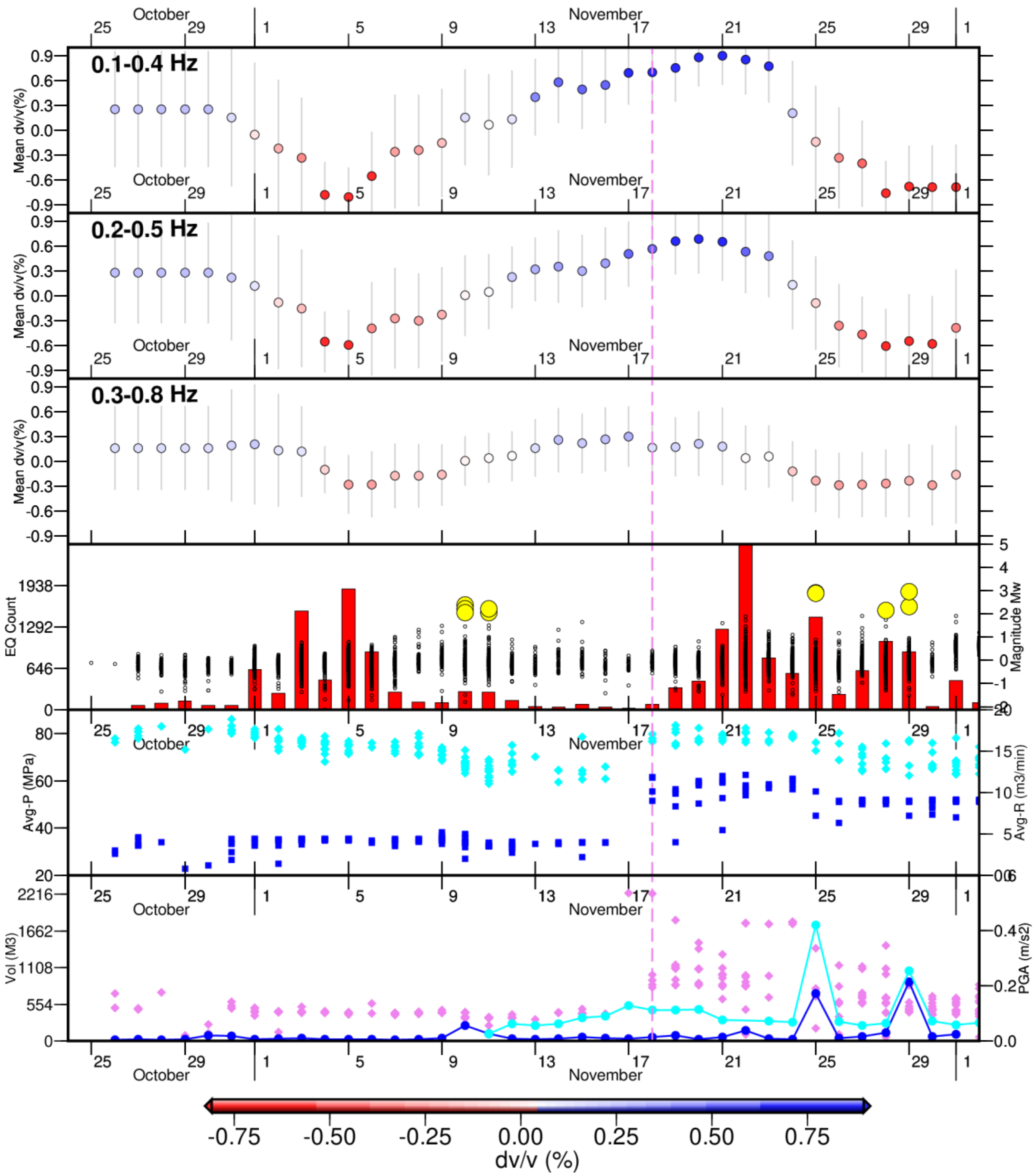

Fig. 5. Comparison of the temporal evolution of dv/v with induced seismicity, injection parameters (injected volume, injection rate, and pressure), and ground motion. The vertical pink dash line demarcates

the end of the first stimulation (well C) and the onset of the second stimulation (well A, B, D). The first three panel shows dv/v measurements at 0.1-0.4, 0.2-0.5, and 0.3-0.8 Hz. The fourth panel from the top shows the temporal evolution of induced earthquakes with more significant events (M2+) highlighted with yellow-colored circles. The fifth panel shows the average injection pressure (cyan diamonds) and injection rate (blue squares). The last panel shows the injected volume (pink diamond) and daily peak ground acceleration (PGA). The navy-blue line and circles show the average PGA from the six broadband seismometers, while the cyan line and circles show the estimated PGA from the accelerometer.

There were two phases of HF stimulations. The first one was performed from October 26 to November 17, 2016, to well C only, while wells A, B, and D were simultaneously stimulated with increased injection rates and pressures from November 18 to December 1, 2016 (Fig. 1; Eaton et al., 2018). Since the goal of HF is to increase the permeability of reservoir rocks by generating fractures via fluid injection, the process alters the poroelastic stress of the subsurface configuration, elevates pore pressures, and consequently generates earthquakes. All these processes further enhance the degree of deformation near the injection wells (Bao and Eaton 2016; Atkinson et al., 2016; Kao et al., 2018a). The daily distribution of induced events shows two broad peaks of intense seismicity during the two stimulation periods that generally correlate with the timing of dv/v reductions. Therefore, we hypothesize that the observed seismic velocity reductions are caused by subsurface deformation (e.g., opening of pores, enhancement of crack density) in response to stress changes induced by fluid overpressures and subsequent ground shaking by swarms of induced events (e.g., Mordret et al., 2016; Taira et al., 2018; Zhang et al., 2020). Possibly due to the smaller magnitudes of induced events and limited ground shaking, there is no clear sign of co-seismic velocity drop similar to those reported for natural earthquakes, even for the most significant induced events (~M3) during the deployment (e.g., Taira et al., 2015; Pei et al., 2019; Wu et al., 2016; Yukutake et al., 2016). Similarly, we did not observe precursory velocity drops preceding the occurrence of induced events like those reported at volcanic edifices (e.g., Brenguier et al., 2008; De Plaen et al., 2016,2018, Yates et al., 2019).

Another essential feature of the dv/v time series is the complete recovery of seismic velocity reduction after the first stimulation. This pattern has been routinely observed following co-seismic dv/v reduction after the occurrence of natural earthquakes (e.g., Brenguier et al., 2008; Pei et al., 2019). However, in our case, the extended period of recovery (a total change of ~ 1.71%) correlates with periods of reduced seismicity and a slight reduction in injection pressure before the onset of intense HF activities in the second stimulation (Fig. 5). Hence, the observed dv/v increases may likely reflect the relaxation process of rock healing, gradual closure of fluid-filled cracks, and re-compaction as the first HF operations wound down (e.g., Brenguier et al., 2008, 2014; Snieder et al., 2016; Taira et al. 2015, 2018). The early decommissioning of the geophones did not allow us to observe the seismic velocity reduction's potential recovery after the second stimulation.

Comparing the first HF phase (well C) to the second (wells A, B, D), we note that the mean number of induced events per day increased from ~128 to ~477, the mean daily injected volume increased from ~433 to ~825 cubic meters, the mean daily injection pressure increased from 72.15 to 75.28 MPa, and the injection rate increased from 3.92 to 10.57 cubic meters per minute. The increased injection of fluid at a higher rate and pressure and stimulation of more wells simultaneously led to an increase in induced seismicity and correspondingly a larger magnitude of dv/v reduction in the second stimulation compared to the first. During the period of intense seismicity, dv/v reduced from 0.25% to -0.81 % (a total change of ~1.06 %) during the first HF phase. A similar drop (from ~0.90% to -0.69%, a total change of ~1.59%) is also observed for the second HF phase.

To further investigate the potential contributions of ground motions due to induced seismicity to the observed dv/v variations, (e.g., Takagi et al., 2012; Yu and Hung, 2012; Hobiger et al., 2016), we compare the temporal evolution of the daily mean dv/v with the daily peak ground acceleration (PGA) averaged from six broadband seismometers and that recorded by an accelerometer collocated with the geophones (Fig. 1 and Fig. 5). Prominent peaks of the mean daily PGA temporally correlate with the relatively larger induced events (M_w larger than 2.0, yellow circles in Fig. 5). They also coincide with periods of dv/v reductions. The observations corroborate our earlier inference that dynamic stresses contribute to the observed dv/v reductions (e.g., Taira et al., 2018; Zhang et al., 2020).

Although several studies have reported a link between dv/v and several meteorological conditions (e.g., Lecocq et al., 2017), it is probably less likely to happen in our case due to the relatively short deployment period (~ 37 days). Similarly, spurious velocity changes related to seasonal variation in the distribution of noise sources can be ruled out (e.g., Zhang et al., 2013).

5. Conclusions

This study uses seismic noise coda wave interferometry to investigate changes in subsurface seismic velocity in response to hydraulic fracturing operations within the Western Canada Sedimentary Basin. The first phase of HF stimulation was performed from October 26 to November 17, 2016, to one well, while three wells were simultaneously stimulated in the second phase with increased injection rates and pressures from November 18 to December 1, 2016. During both HF stimulations, we observe seismic velocity changes with amplitudes that increase with decreasing frequency. Specifically, two time periods of velocity reductions appear after many induced earthquakes during the well stimulations. However, much larger numbers of induced events and more significant dv/v reductions are observed in the second stimulation with increased injection volume, pressure, and rate. An extended period of velocity increase correlates with reduced induced seismicity towards the end of the first stimulation. Considering all the temporal comparisons that we have examined; we conclude that the observed dv/v reduction is likely caused by ground deformation due to fluid injection and ground motion from induced earthquakes. On the other hand, increases in dv/v are associated with postseismic recovery processes indicating periods of crustal strengthening. Our study shed new light on subsurface structural changes induced by hydraulic fracturing operations and provides valuable new information that can be potentially useful for seismic hazard study in the region.

Acknowledgments

We thank the sponsors and participants of the ToC2ME program for the seismic data used in this study. Continuous ambient noise data were retrieved from IRIS Data Management Centre (see also the ToC2ME GitHub: https://github.com/ToC2ME/). We used the seismicity catalog developed by (Igonin et al., 2020), which is publicly available (https://zenodo.org/record/3900657). Well completions and fracking data were obtained from the geoLOGIC frac database (www.gdcweb.geologic.com; Last accessed July 2020). This research is partially supported by the Environmental Geoscience Program of NRCan, a NSERC Discovery grant (RGPIN-201904148), and a grant from Geoscience BC (2019-0007a).

References

Alberta Energy Regulator (2015). Subsurface order no. 2: Monitoring and reporting of seismicity in the vicinity of hydraulic fracturing operations in the Duvernay zone, Fox Creek, Alberta. *AER bulletin 2015–07* (pp. 3). https://aer.ca/documents/orders/subsurface-orders/ SO2.pdf

Amann, F., Gischig, V., Evans, K., Doetsch, J., Jalali, R., Valley, B., et al. (2018). The seismo-hydromechanical behavior during deep geothermal reservoir stimulations: Open questions tackled in a decameter-scale in situ stimulation experiment. *Solid Earth*, *9*(1), 115–137. https://doi.org/10.5194/se-9-115-2018

Atkinson, G. M., Eaton, D. W., and Igonin, N. (2020). Developments in understanding seismicity triggered by hydraulic fracturing. *Nature Reviews Earth and Environment*, 1–14. https://doi.org/10.1038/s43017-020-0049-7

Atkinson, G. M., Eaton, D. W., Ghofrani, H., Walker, D., Cheadle, B., Schultz, R., et al. (2016). Hydraulic fracturing and seismicity in the Western Canada Sedimentary Basin. *Seismological Research Letters*, *87*(3), 631–647. https://doi.org/10.1785/0220150263

Atkinson, G. M., Eaton, D. W., Ghofrani, H., Walker, D., Cheadle, B., Schultz, R., ... and Liu, Y. (2016). Hydraulic fracturing and seismicity in the Western Canada Sedimentary Basin. *Seismological Research Letters*, 87(3), 631-647, doi: 10.1785/0220150263.

Babaie Mahani, A., Kao, H., Walker, D., Johnson, J., and Salas, C. (2016). Performance evaluation of the regional seismograph network in northeast British Columbia, Canada, for monitoring of induced seismicity. *Seismological Research Letters*, *87*(3), 648–660. https://doi.org/10.1785/0220150241

Babaie Mahani, A., Schultz, R., Kao, H., Walker, D., Johnson, J., and Salas, C. (2017). Fluid injection and seismic activity in the northern Montney Play, British Columbia, Canada, with special reference to the 17 August 2015 Mw 4.6 induced earthquake. *Bulletin of the Seismological Society of America*, *107*(2), 542–552. https://doi.org/10.1785/0120160175

Bao, X. W., and Eaton, D. W. (2016). Fault activation by hydraulic fracturing in western Canada. *Science*, *354*(6318), 1406–1409. https://doi.org/10.1126/science.aag,2583

Bensen, G. D., Ritzwoller, M. H., Barmin, M. P., Levshin, A. L., Lin, F., Moschetti, M. P., ... and Yang, Y. (2007). Processing seismic ambient noise data to obtain reliable broad-band surface wave dispersion measurements. *Geophysical Journal International*, *169*(3), 1239-1260.

Brenguier, F., Campillo, M., Hadziioannou, C., Shapiro, N. M., Nadeau, R. M., and Larose, E. (2008). Postseismic relaxation along the San Andreas fault at Parkfield from continuous seismological observations. *Science*, 321(5895), 1478-1481.

Brenguier, F., Campillo, M., Takeda, T., Aoki, Y., Shapiro, N. M., Briand, X., et al. (2014). Mapping pressurized volcanic fluids from induced crustal seismic velocity drops. *Science*, 345(6192), 80-82.

Brenguier, F., Kowalski, P., Ackerley, N., Nakata, N., Boué, P., Campillo, M., et al. (2016). Toward 4D noise-based seismic probing of volcanoes: Perspectives from a large-N experiment on Piton de la Fournaise volcano. *Seismological Research Letters*, 87(1), 15–25. https://doi.org/10.1785/0220150173

Brenguier, F., Campillo, M., Hadziioannou, C., Shapiro, N. M., Nadeau, R. M., and Larose, E. (2008). Postseismic relaxation along the San Andreas fault at Parkfield from continuous seismological observations. *science*, *321*(5895), 1478-1481.

Chadwick, A., Williams, G., Delepine, N., Clochard, V., Labat, K., Sturton, S., ... and Rossi, G. (2010). Quantitative analysis of time-lapse seismic monitoring data at the Sleipner CO 2 storage operation. *The Leading Edge*, *29*(2), 170-177.

Civilini, F., Savage, M. K., and Townend, J. (2020). Shear wave velocity changes induced by earthquakes and rainfall at the Rotokawa and Ngatamariki geothermal fields, Taupō Volcanic Zone, New Zealand. *Geophysical Journal International*, *221*(1), 97-114.

Clarke, D., L. Zaccarelli, N. M. Shapiro, and F. Brenguier (2011), Assessment of resolution and accuracy of the Moving Window Cross Spectral technique for monitoring crustal temporal variations using ambient seismic noise, *Geophysical Journal International*, 186(2), 867–882.

Clements, T., and Denolle, M. A. (2018). Tracking groundwater levels using the ambient seismic field. *Geophysical Research Letters*, 45 (13), 6459-6465.

De Plaen, R. S., Cannata, A., Cannavo, F., Caudron, C., Lecocq, T., and Francis, O. (2019). Temporal changes of seismic velocity caused by volcanic activity at mt. etna revealed by the autocorrelation of ambient seismic noise. *Frontiers in Earth Science*, 6 , 251.

De Plaen, R.S.M., Lecocq, T., Caudron, C., Ferrazzini, V., Francis, O., 2016. Single-station monitoring of volcanoes using seismic ambient noise. *Geophysical Research Letters*, 43: 8511-8518.

Doetsch, J., Gischig, V. S., Villiger, L., Krietsch, H., Nejati, M., Amann, F., et al. (2018). Subsurface fluid pressure and rock deformation monitoring using seismic velocity observations. *Geophysical Research Letters*, *45*, 10,389–10,397. https://doi.org/10.1029/2018GL079009

Donaldson, C., Caudron, C., Green, R. G., Thelen, W. A., and White, R. S. (2017). Relative seismic velocity variations correlate with deformation at Kīlauea volcano. *Science advances*, *3*(6), e1700219.

Eaton, D. W., Igonin, N., Poulin, A., Weir, R., Zhang, H., Pellegrino, S., and Rodriguez, G. (2018). Induced seismicity characterization during hydraulic fracture monitoring with a shallow-wellbore geophone array and broadband sensors. *Seismological Research Letters*, *89*(5), 1641–1651. https://doi.org/10.1785/0220180055

Ellsworth, W. L. (2013). Injection-Induced Earthquakes. *Science*, *341*, 1225942. https://doi.org/10.1126/science.1225942

Froment, B., Campillo, M., Chen, J.H. and Liu, Q.Y. (2013) Deformation at depth associated with the 12 May 2008 MW 7.9 Wenchuan earthquake from seismic ambient noise monitoring. *Geophysical Research Letters*, 40, 78–82.doi:10.1029/2012GL053995

Ghofrani, H., and Atkinson, G. M. (2016). A preliminary statistical model for hydraulic fracture-induced seismicity in the Western Canada Sedimentary basin. *Geophysical Research Letters*, *43*(19), 10-164.

Ghofrani, H., and Atkinson, G. M. (2020). Activation rate of seismicity for hydraulic fracture wells in the Western Canada Sedimentary Basin. *Bulletin of the Seismological Society of America*, *110*(5), 2252–2271. https://doi.org/10.1785/0120200002

Grêt, A., Snieder, R. and Scales, J. (2006) Time-lapse monitoring of rock properties with coda wave interferometry. *J. Geophys. Res. Solid Earth*, 111. doi:10.1029/2004JB003354

Hadziioannou, C., Larose, E., Baig, A.M., Roux, P. and Campillo, M. (2011) Improving temporal resolution in ambient noise monitoring of seismic wave speed. *J. Geophys. Res. Solid Earth*, 116. doi:10.1029/2011JB008200

Hadziioannou, C., Larose, E., Coutant, O., Roux, P. and Campillo, M. (2009) Stability of Monitoring Weak Changes in Multiply Scattering Media with Ambient Noise Correlation: *Laboratory Experiments*, 1–10. doi:10.1121/1.3125345

Hillers, G., Campillo, M., Brenguier, F., Moreau, L., Agnew, D. and Ben-Zion, Y. (2019) Seismic Velocity Change Patterns Along the San Jacinto Fault Zone Following the 2010 M 7.2 El Mayor-Cucapah and M 5.4 Collins Valley Earthquakes. *J. Geophys. Res. Solid Earth*. doi:10.1029/2018jb017143

Hobiger, M., Wegler, U., Shiomi, K., and Nakahara, H. (2016). Coseismic and post-seismic velocity changes detected by Passive Image Interferometry: Comparison of one great and five strong earthquakes in Japan. *Geophysical Journal International*, *205*(2), 1053–1073. https://doi.org/10.1093/gji/ggw066

Hui, G., Chen, S., Chen, Z., and Gu, F. (2021). An integrated approach to characterize hydraulic fracturing-induced seismicity in shale reservoirs. *Journal of Petroleum Science and Engineering*, *196*(2021), 107624. https://doi.org/10.1016/j.petrol.2020.107624

Hui, G., Chen, S., Gu, F., Pang, Y., Yu, X., and Zhang, L. (2021). Insights on controlling factors of hydraulically induced seismicity in the Duvernay East Shale Basin. *Geochemistry, Geophysics, Geosystems*, 22, e2020GC009563. https://doi.org/10.1029/2020GC009563

Igonin, N., Zecevic, M., and Eaton, D. W. (2018). Bilinear magnitude-frequency distributions and characteristic earthquakes during hydraulic fracturing. *Geophysical Research Letters*, *45*(23), 12-866.

Igonin, N., Verdon, J. P., Kendall, J. M., and Eaton, D. W. (2020). Large-scale fracture systems are permeable pathways for fault activation during hydraulic fracturing. *Journal of Geophysical Research: Solid Earth*, e2020JB020311.

Ikuta, R., and Yamaoka, K. (2004). Temporal variation in the shear wave anisotropy detected using the Accurately Controlled Routinely Operated Signal System (ACROSS). *Journal of Geophysical Research: Solid Earth*, *109*(B9).

James, S. R., Knox, H. A., Abbott, R. E., and Screaton, E. J. (2017). Improved moving window cross-spectral analysis for resolving large temporal seismic velocity changes in permafrost. *Geophysical Research Letters*, *44*, 4018–4026. https://doi.org/10.1002/2016GL072468

Kao, H., Eaton, D. W., Atkinson, G. M., Maxwell, S., and Mahani, A. B. (2016). Technical meeting on the traffic light protocols (TLP) for induced seismicity: summary and recommendations. In *Geological Survey of Canada, Open File, 8075*. Victoria, Canada: Geological Survey of Canada.

Kao, H., Hyndman, R., Jiang, Y., Visser, R., Smith, B., and Babaie Mahani, A. et al. (2018). Induced Seismicity in Western Canada Linked to Tectonic Strain Rate: Implications for Regional Seismic Hazard. *Geophysical Research Letters*, 45(20). https://doi.org/10.1029/2018gl079288

Kao, H., Visser, R., Smith, B., and Venables, S. (2018). Performance assessment of the induced seismicity traffic light protocol for northeastern British Columbia and western Alberta. *The Leading Edge*, *37*(2), 117–126. https://doi.org/10.1190/tle37020117.1

Kortink, M. (2020). Effect of the Kaikōura Earthquake on Velocity Changes In and Around the Ruptured Region: A Noise Cross-Correlation Approach. MSc. Victoria University of Wellington.

Larose, E., Derode, A., Campillo, M., and Fink, M. (2004). Imaging from one-bit correlations of wideband diffuse wave fields. *Journal of Applied Physics*, *95*(12), 8393-8399.

Lecocq, T., Caudron, C., and Brenguier, F. (2014). MSNOise, a python package for monitoring seismic velocity changes using ambient seismic noise. *Seismological Research Letters*, *85*(3), 715–726. https://doi.org/10.1785/0220130073

Lecocq, T., Longuevergne, L., Pedersen, H. A., Brenguier, F., and Stammler, K. (2017). Monitoring ground water storage at mesoscale using seismic noise: 30 years of continuous observation and thermo-elastic and hydrological modeling. *Scientific Reports*, *7*(1), 1–16. https://doi.org/10.1038/s41598-017-14468-9

Levshin, A. L., T. B. Yanovskaya, A. V. Lander, B. G. Bukchin, M. P. Barmin, L. I. Ratnikova, and E. N. (1989). Seismic surface waves in a laterally inhomogeneous Earth. Kluwer Academic Publishers.

Lobkis, O. I., and Weaver, R. L. (2001). On the emergence of the Green's function in the correlations of a diffuse field. *The Journal of the Acoustical Society of America*, *110*(6), 3011-3017.

Lobkis, O. I., and Weaver, R. L. (2003). Coda-wave interferometry in finite solids: Recovery of P-to-S conversion rates in an elastodynamic billiard. *Physical review letters*, *90*(25), 254302.

Mao, S., Campillo, M., Hilst, R.D. van der, Brenguier, F., Stehly, L. and Hillers, G. (2019). High Temporal Resolution Monitoring of Small Variations in Crustal Strain by Dense Seismic Arrays. *Geophysical Research Letters*, 46, 128–137. doi:10.1029/2018GL079944

Mikesell, T.D., Malcolm, A.E., Yang, D. and Haney, M.M. (2015) A comparison of methods to estimate seismic phase delays: Numerical examples for coda wave interferometry. *Geophysical Journal International*, 202, 347–360. doi:10.1093/gji/ggv138

Mordret, A., Mikesell, T. D., Harig, C., Lipovsky, B. P., and Prieto, A. (2016). Monitoring south-west Greenland's ice sheet melt with ambient seismic noise. *Science Advances*, *2*(5), e1501538. https://doi.org/10.1126/sciadv.1501538

Nakata, N., and Snieder, R. (2012). Estimating near-surface shear wave velocities in Japan by applying seismic interferometry to KiK-net data. *Journal of Geophysical Research*, *117*, B01308. https://doi.org/10.1029/2011JB008595

Nimiya, H., Ikeda, T., and Tsuji, T. (2017). Spatial and temporal seismic velocity changes on Kyushu Island during the 2016 Kumamoto earthquake. *Science advances*, *3*(11), e1700813.

Niu, F., Silver, P.G., Daley, T.M., Cheng, X. and Majer, E.L. (2008). Preseismic velocity changes observed from active source monitoring at the parkfield SAFOD drill site, *Nature,* 454, 204–208. doi:10.1038/nature07111.

Obermann, A., B. Froment, M. Campillo, E. Larose, T. Planès, B. Valette, J. H. Chen, and Q. Y. Liu (2014), Seismic noise correlations to image structural and mechanical changes associated with the Mw 7.9 2008 Wenchuan earthquake, *J. Geophys. Res. Solid Earth*, 119, 3155–3168, doi:10.1002/2013JB010932.

Obermann, A., Planès, T., Hadziioannou, C., and Campillo, M. (2016). Lapse-time-dependent coda-wave depth sensitivity to local velocity perturbations in 3-D heterogeneous elastic media. *Geophysical Journal International*, 207(1), 59–66. https://doi.org/10.1093/gji/ggw264

Obermann, A., Planès, T., Larose, E., Sens-Schönfelder, C., and Campillo, M. (2013). Depth sensitivity of seismic coda waves to velocity perturbations in an elastic heterogeneous medium. *Geophysical Journal International*, 194(1), 372–382. https://doi.org/10.1093/gji/ggt043

Olivier, G. and Brenguier, F. (2016). Interpreting seismic velocity changes observed with ambient seismic noise correlations. *Interpretation*, vol. 4(3), pp. SJ77-SJ85. DOI: 10.1190/INT-2015-0203.1

Olivier, G., Brenguier, F., Carey, R., Okubo, P., and Donaldson, C. (2019). Decrease in seismic velocity observed prior to the 2018 eruption of Kīlauea Volcano with ambient seismic noise interferometry. *Geophysical Research Letters*, 46(7), 3734- 3744.

Pawley, S., Schultz, R., Playter, T., Corlett, H., Shipman, T., and Lyster, S. (2018). The geological susceptibility of induced earthquakes in the Duvernay play. *Geophysical Research Letters*, *45*(4), 1786–1793. https://doi.org/10.1002/2017GL076100

Pei, S., Niu, F., Ben-Zion, Y., Sun, Q., Liu, Y., Xue, X., ... and Shao, Z. (2019). Seismic velocity reduction and accelerated recovery due to earthquakes on the Longmenshan fault. *Nature Geoscience*, *12*(5), 387-392

Pezzo, G., De Gori, P., Lucente, F. P., and Chiarabba, C. (2018). Pore pressure pulse drove the 2012 Emilia (Italy) series of earthquakes. *Geophysical Research Letters*, *45*, 682–690. https://doi.org/10.1002/2017GL076110

Poulin, A., Weir, R., Eaton, D., Igonin, N., Chen, Y., Lines, L., and Lawton, D. (2019). Focal-time analysis: A new method for stratigraphic depth control of microseismicity and induced seismic events. *Geophysics*, *84*(6), KS173-KS182.

Poupinet, G., Ellsworth, W. L., and Frechet, J. (1984). Monitoring velocity variations in the crust using earthquake doublets: An application to the Calaveras Fault, California. Journal of Geophysical Research: Solid Earth, 89(B7), 5719-5731.

Qin, L., Y. Ben-Zion, L. F. Bonilla and J. H. Steidl, 2020. Imaging and monitoring temporal changes of shallow seismic velocities at the Garner Valley near Anza, California, in relation to the M7.2 2010 El Mayor-Cucapah earthquake, *J. Geophys., Res.,* 125, e2019JB018070, doi: 10.1029/2019JB018070.

Qiu, H., Hillers, G., and Ben-Zion, Y. (2020). Temporal changes of seismic velocities in the San Jacinto Fault zone associated with the 2016 M w 5.2 Borrego Springs earthquake. *Geophysical Journal International*, *220*(3), 1536-1554.

Ratdomopurbo, A., and Poupinet, G. (1995). Monitoring a temporal change of seismic velocity in a volcano: Application to the 1992 eruption of Mt. Merapi (Indonesia). *Geophysical research letters*, *22*(7), 775-778.

Roux, P. and Ben-Zion, Y., 2013. Monitoring fault zone environments with correlations of earthquake waveforms, *Geophysical Journal International,* 196(2), 1073–1081, doi:10.1093/gji/ggt441.

Schultz, R., Atkinson, G., and Eaton, D. W. (2018). Hydraulic fracturing volume is associated with induced earthquake productivity in the Duvernay play. *Science*, *359*(6373), 304–308. https://doi.org/10.1126/science.aao0159.

Schultz, R., Skoumal, R. J., Brudzinski, M. R., Eaton, D., Baptie, B., and Ellsworth, W. (2020). Hydraulic fracturing-induced seismicity. *Reviews of Geophysics*, *58*(3). e2019RG000695. https://doi.org/10.1029/2019RG000695

Schultz, R., Stern, V., Novakovic, M., Atkinson, G., and Gu, Y. J. (2015). Hydraulic fracturing and the Crooked Lake Sequences: Insights gleaned from regional seismic networks. *Geophysical Research Letters*, *42*(8), 2750–2758. https://doi.org/10.1002/2015GL063455

Schultz, R., Wang, R., Gu, Y. J., Haug, K., and Atkinson, G. (2017). A seismological overview of the induced earthquakes in the Duvernay play near Fox Creek, Alberta. *Journal of Geophysical Research: Solid Earth*, *122*(1), 492–505. https://doi.org/10.1002/2016JB013570

Sens-Schönfelder, C., and Larose, E. (2008). Temporal changes in the lunar soil from correlation of diffuse vibrations. *Physical Review E*, *78*(4), 045601.

Sens-Schönfelder, C., and Wegler, U. (2006). Passive image interferometry and seasonal variations of seismic velocities at Merapi Volcano, Indonesia. *Geophysical research letters*, *33*(21).

Sens-Schönfelder, C., Pomponi, E., and Peltier, A. (2014). Dynamics of Piton de la Fournaise volcano observed by passive image interferometry with multiple references. *Journal of Volcanology and Geothermal Research*, *276*, 32-45.

Shapiro, N. M., and Campillo, M. (2004). Emergence of broadband Rayleigh waves from correlations of the ambient seismic noise. *Geophysical Research Letters*, *31*(7).

Snieder, R., Grêt, A., Douma, H., and Scales, J. (2002). Coda wave interferometry for estimating nonlinear behavior in seismic velocity. *Science*, *295*(5563), 2253-2255.

Snieder, R., Sens-Schönfelder, C., and Wu, R. (2016). The time dependence of rock healing as a universal relaxation process, a tutorial. *Geophysical Journal International*, 208(1), 1-9.

Stehly, L., Campillo, M., and Shapiro, N. M. (2006). A study of the seismic noise from its long-range correlation properties. *Journal of Geophysical Research: Solid Earth*, *111*(B10).

Taira, T. A., F. Brenguier, and Q. Kong (2015), Ambient noise-based monitoring of seismic velocity changes associated with the 2014 Mw 6.0 South Napa earthquake, *Geophys. Res. Lett*., 42, 6997–7004, doi:10.1002/2015GL065308.

Taira, T. A., Nayak, A., Brenguier, F., and Manga, M. (2018). Monitoring reservoir response to earthquakes and fluid extraction, Salton Sea geothermal field, California. *Science Advances*, 4(1), e1701536.

Taira, T., and F. Brenguier (2016). Response of hydrothermal system to stress transients at Lassen Volcanic Center, California, inferred from seismic interferometry with ambient noise, *Earth, Planets, and Space*, *68*, 162, doi:10.1186/s40623-016-0538-6.

Takagi, R., T. Okada, H. Nakahara, N. Umino, and A. Hasegawa (2012), Coseismic velocity change in and around the focal region of the 2008 Iwate-Miyagi Nairiku earthquake, *J. Geophys. Res*., 117, B06315, doi:10.1029/2012JB009252.

Tan, F., Kao, H., Nissen, E., and Eaton, D. (2019). Seismicity-Scanning Based on Navigated Automatic Phase-Picking. *Journal of Geophysical Research: Solid Earth*, 124(4), 3802-3818. https://doi.org/10.1029/2018jb017050

Taylor, G., and Hillers, G. (2020). Estimating temporal changes in seismic velocity using a Markov chain Monte Carlo approach. *Geophysical Journal International*, *220*(3), 1791-1803.

Tribaldos, V. R., and Ajo-Franklin, J. B. Aquifer Monitoring Using Ambient Seismic Noise Recorded with Distributed Acoustic Sensing (DAS) Deployed on Dark Fiber. *Journal of Geophysical Research: Solid Earth*, e2020JB021004.

Vaezi, Y., and Van der Baan, M. (2019). Interferometric time-lapse velocity analysis: application to a salt-water disposal well in British Columbia, Canada. *Geophysical Journal International*, *219*(2), 834-852.

Wang, Q. Y., Brenguier, F., Campillo, M., Lecointre, A., Takeda, T., and Aoki, Y. (2017). Seasonal crustal seismic velocity changes throughout Japan. *Journal of Geophysical Research: Solid Earth*, *122*, 7987–8002. https://doi.org/10.1002/2017JB014307

Wu, C., Delorey, A., Brenguier, F., Hadziioannou, C., Daub, E.G. and Johnson, P. (2016). Constraining depth range of S wave velocity decrease after large earthquakes near Parkfield, California. *Geophysical Research Letters*, vol. 43(12), pp. 6129-6136. DOI: 10.1002/2016GL069145

Wu, S. M., Lin, F. C., Farrell, J., Shiro, B., Karlstrom, L., Okubo, P., and Koper, K. (2020). Spatiotemporal seismic structure variations associated with the 2018 Kīlauea eruption based on temporary dense geophone arrays. *Geophysical Research Letters*, *47*(9), e2019GL086668.

Yates, A. S., Savage, M. K., Jolly, A. D., Caudron, C., Hamling, I. J., 2019. Volcanic, coseismic, and seasonal changes detected at White Island (Whakaari) volcano, New Zealand, using seismic ambient noise. *Geophys. Res. Lett*., 46, 99-108.

Yu, T. C., and Hung, S. H. (2012). Temporal changes of seismic velocity associated with the 2006 Mw 6.1 Taitung earthquake in an arc-continent collision suture zone. *Geophysical Research Letters*, 39(12), L12307.

Yu, W., Lin, J.-T., Su, J., Song, T.-R. A., and Kang, C.-C. (2020). S coda and Rayleigh waves from a decade of repeating earthquakes reveal discordant temporal velocity changes since the 2004 Sumatra earthquake. *Journal of Geophysical Research: Solid Earth*, 125, e2020JB019794. https://doi.org/10.1029/2020JB019794

Yukutake, Y., Ueno, T., and Miyaoka, K. (2016). Determination of temporal changes in seismic velocity caused by volcanic activity in and around Hakone volcano, central Japan, using ambient seismic noise records. *Progress in Earth and Planetary Science*, *3*(1), 1-14.

Zelt, C. A., and Ellis, R. M. (1989). Seismic structure of the crust and upper mantle in the Peace River Arch region, Canada. *Journal of Geophysical Research: Solid Earth*, *94*(B5), 5729-5744.

Zhan, Z., Tsai, V. C., and Clayton, R. W. (2013). Spurious velocity changes caused by temporal variations in ambient noise frequency content. *Geophysical Journal International*, *194*(3), 1574-1581.

Zhang, Y., Niu, F., Tao, K., Ning, J., Chen, H., and Tang, Y. (2020). Hydraulic injection-induced velocity changes revealed by surface wave coda and polarization data at a shale play site in southwest China. *Journal of Geophysical Research: Solid Earth*, 125, e2019JB019169. https://doi.org/10.1029/2019JB019169